PCCP

Accepted Manuscript

1　**Tuning the carrier concentration using Zintl chemistry in Mg_3Sb_2 and, its**

2　**implications on thermoelectric figure-of-merit**

3

4　A. Bhardwaj[1, 2], N. S. Chauhan[1,2], S. Goel[1,2], Vijeta Singh[1,3] J. J. Pulikkotil[1,3,4], T.D.

5　Senguttuvan[1,2], and D. K. Misra[1,2*]

6

7　[1]Academy of Scientific & Innovative Research (AcSIR), CSIR-National Physical Laboratory

8　(CSIR-NPL) campus, New Delhi-110012, India.

9　[2]Physics of Energy Harvesting Division, National Physical Laboratory, Council of Scientific and

10　Industrial Research, New Delhi 110012, India.

11　[3]Quantum Phenomena & Applications Division, National Physical Laboratory, Council of

12　Scientific and Industrial Research, New Delhi 110012, India.

13　[4]Computational and Networking facility, National Physical Laboratory, Council of Scientific and

14　Industrial Research, New Delhi 110012, India

15　## Abstract:

16　Zintl compounds are potential candidates for efficient thermoelectric materials, because they are

17　typically small band gap semiconductors. In addition, such compounds allow fine tuning of

18　carrier concentration by chemical doping for the optimization of thermoelectric performance.

19　Herein, such tunability is demonstrated in Mg_3Sb_2- based Zintl compound via. Zn^{2+} doping at

20　Mg^{2+} site of the anionic framework $(Mg_2Sb_2)^{2-}$, in the series $Mg_{3-x}Zn_xSb_2$ $(0 \leq x \leq 0.1)$. The

21　materials have been successfully synthesized by spark plasma sintering (SPS) technique. The X-

22　ray diffraction (XRD) analysis confirms single solid solution phase of $Mg_{3-x}Zn_xSb_2$ $(0 \leq x \leq 0.1)$.

23　The thermoelectric properties are characterized by Seebeck coefficient, electrical conductivity,

24　and thermal conductivity measurements from 323 K to 773 K. The isoelectronic Zn substitution

25　at Mg site presents the controlled variation in the carrier concentration for optimizing high power

26　factor and reduced thermal conductivity. These results lead to a substantial increase in ZT of 0.37

27　at 773 K for a composition with x=0.10 which is ~ 42 % higher than undoped Mg_3Sb_2. The

28　electronic transport data of $Mg_{3-x}Zn_xSb_2$ $(0 \leq x \leq 0.1)$ compound are analyzed using a single

29　parabolic band model predicting that $Mg_{2.9}Zn_{0.1}Sb_2$ exhibits near-optimal carrier concentration

1 for high ZT. The electronic structure of transport properties of these disordered $Mg_{3-x}Zn_xSb_2$ ($0 \leq$

2 $x \leq 0.1$) are also studied by density functional theory and the results obtained are in good

3 agreement with experimental results. The low cost, lightness and non-toxicity of the constituents

4 elements make these materials ideal for mid-temperature thermoelectric applications.

5 *Corresponding author. E-mail address: misradk@nplindia.org, dakkmisra@gmail.com (DKM)

6 1. Introduction

7 Carrier concentration (n) appears as a fundamental entity to all three basic quantities

8 through which the thermoelectric figure-of-merit is defined.[1] While Seebeck coefficient (S) is

9 inversely proportional to n, (S $\propto n^{-2/3}$), a linear dependence of n is derived for electrical

10 conductivity (σ) following the classical Drude model and, also for thermal conductivity (κ) when

11 expressed through the Wiedemann-Franz's law. Evidently optimizing n, therefore becomes an

12 important challenge in gauging the performance of a thermoelectric materials and the same has

13 been demonstrated in various class of thermoelectric materials.[2-11]

14 The conventional strategy to tune carrier concentration is usually accomplished via near

15 group elemental doping of the chemical periodic table. However, for Zintl compounds which are

16 promising thermoelectric materials,[12-20] this conventional strategy is detrimental since they are

17 charge balanced systems. The delicate balance of the ionic and covalent interactions in these

18 Zintl systems make the dopants very selective in its nature and concentration. Hence doping is

19 accomplished only over a very narrow compositional homogeneity range in its materials phase

20 diagram.

21 Along these perspectives, we explore the possible routes to optimize the carrier

22 concentration and its effects on the thermoelectric properties of the Zintl compound Mg_3Sb_2,

23 which crystallizes in the anti-La_2O_3 structure.[21] The underlying hexagonal symmetry (space

24 group P$\bar{3}$m1) distinguishes two Mg ions, denoted as Mg(I) and Mg(II),which occupy the

25 octahedral (1b) and tetrahedral sites (2d) with Wyckoff positions $(0,0,\frac{1}{2})$ and $(\frac{1}{2}, \frac{2}{3}, z_{Mg})$,

26 respectively, with Sb ions at $(\frac{1}{2}, \frac{2}{3}, z_{Sb})$. The Mg (I) ions form a two dimensional layered cation

27 layer stacked along the c-axis, between which the $(Mg_2Sb_2)^{2-}$ substructures form the anionic

28 network. This covalently bound anion substructure enables high carrier mobilities. The

29 underlying aspect of the Zintl chemistry in this material is that the ionic cations (Mg) donate

30 electrons to the covalently bound anion framework. Hence in such systems, the cationic sites

1   could be subjected to chemical substitutions for carrier concentration tuning, as well as, to a

2   certain extent, enhancing phonon scattering depending on the mass of the dopant. The schematic

3   diagram of the crystal structure of β-Mg_3Sb_2 is shown in the figure 1. The crystal structure of β-

4   Mg_3Sb_2 consists of Mg^{2+} cations layers (the octahedral position in the lattice) that donate the

5   electrons to the $[Mg_2Sb_2]^{2-}$ framework (the tetrahedral position in the lattice) similar to the

6   structure of $CaAl_2Si_2$.[22]
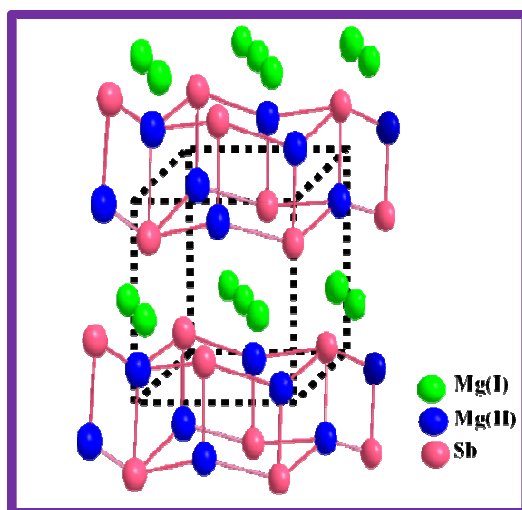
7

8   **Figure 1:** Schematic diagram of crystal structure of β-Mg_3Sb_2 showing the anionic framework of

9    $[Mg_2Sb_2]^{2-}$ with double layer and Mg^{2+} cations between the layers.

10

11   Interestingly, we note from our earlier studies that the two Mg ions in Mg_3Sb_2 display

12   different bonding characteristics between the Mg(I)-Sb and Mg(II)-Sb bonds.[18] Thus,

13   isoelectronic species such as Zn replacing Mg in Mg_3Sb_2 could be expected to be site selective.

14   In case, if the choice of the species is such that the polarity in the anionic substructure could be

15   reduced, then that would ensure enhancement in the thermoelectric properties of the material.

16   Besides, what qualifies Mg_3Sb_2 as a promising thermoelectric material is its semiconducting

17   properties, with an electronic band gap (E_G) $\simeq$ 0.6-0.8 eV.[23] Subsequently, an empirical estimate

18   of its operating temperature (T_O) according to the $E_G = 10K_BT_O$ rule ($K_B \equiv$ Boltzmann constant),

19   finds T_O in the range of $\simeq$ 700 - 900 K. Further, chemical disorder which would induce band

20   broadening is certainly expected to reduce E_G, and so it's operating temperature.

21   The thermoelectric properties of Mg_3Sb_2 at high temperature have been studied by

22   several groups.[24-28] However, several difficulties such as formation of single phase[25,26] and the

presence of oxygen at grain boundaries[27] have hindered the progress of the material towards its viability for thermoelectric applications. However, adopting to a different synthesis route by using spark plasma sintering (SPS), a near-stoichiometric single phase Mg_3Sb_2 could be obtained.[18] Iso-electronic substitution of Bi at Sb site in $Mg_3Sb_{2-x}Bi_x$ and Pb doping in the anionic framework of Mg_3Sb_2 have been also studied for optimization of high ZT.[18,20] These experiments reveals that the enhancement in ZT is attributed to the best control in carrier concentration.[18,20] Moreover, recent theoretical investigation of Mg_3Sb_2 and a series of compounds $AeMg_2Pn_2$ (Ae = Ca, Sr, Ba; Pn= As, Sb, Bi) compounds,[29] also show that optimization of the carrier concentration play an important role to enhance the thermoelectric properties of these compounds. Thus overall, we believe that isoelectronic Zn substitution on Mg-site in Mg_3Sb_2 will not only optimize the carrier concentration but such doping is expected to bring substantial change in the chemical bonding, affecting the physical and chemical properties of the system.

With Zn^{2+} substitutions in Mg_3Sb_2, we find changes in the carrier concentration leading to a substantial enhancement in ZT, scaling up to $\simeq$ 42 % in comparison with the undoped Mg_3Sb_2. The increase in the Seebeck coefficient and decrease in its operating temperature is in good accordance with the phenomenological models. Further, to understand the change in the structural, electronic and transport properties in Mg_3Sb_2 with Zn substitutions, calculations were also carried out within the framework of density functional theory. The theoretical results are good agreement with the experiments.

2. Experimental Procedures:

2.1. Materials Processing and Densification

Stoichiometric amounts of high purity elements magnesium (Mg; 99.99%, Alfa Aesar), antimony (Sb; 99.99%, Alfa Aesar), and zinc (Zn; 99.99%, Alfa Aesar) for synthesizing $Mg_{3-x}Zn_xSb_2$ ($0 \leq x \leq 0.1$) were blended in mechanical milling and subsequently grounded in an agate mortar. The blended powders were then subjected to SPS at temperature 1073 K and a pressure of 50 MPa with a holding time of 10 minutes. This procedure yields pellets of 12.7 mm diameter and 2.5 mm thick. The SPS were performed in high vacuum and therefore eliminates adsorptive gases

1   and impurities existing on the surface of the powder particles, and also oxidation resulting in

2   very clean samples. The SPS of the powder materials involves simultaneous melting reaction and

3   consolidation resulting a single phase precipitation. The present synthesis strategy involving

4   direct rapid heating reaction and consolidation in SPS followed by fast cooling, result to form

5   nanosized grains of $Mg_{3-x}Zn_xSb_2$ ($0 \leq x \leq 0.1$) samples.

6

7   **2.2. Structural Characterization**

8   The gross structural characterization of $Mg_{3-x}Zn_xSb_2$ ($0 \leq x \leq 0.1$) samples were carried out by

9   powder X-ray diffractometer (Rigaku Mini Flex II) in reflection θ- 2θ geometry, with position

10   sensitive detector (Ultafast D Tex), operating at 30 kV and 20 mA, using a graphite

11   monochromator and CuK_α radiation with wavelength $\lambda \approx 1.5406$ Å along with $CuK_{\alpha2}$ filter and

12   rotating anode equipped with powder 2θ diffractometer ranging from 20˚ to 80˚. The

13   experimental conditions and parameters such as sample size, power ratings of X-ray tube (30 kV,

14   20 mA) and other diffractometer parameters such as scan speed, counting steps etc. were kept

15   constant for all diffraction experiments.

16   The microstructure investigation of best performing SPSed sample ($Mg_{2.9}Zn_{0.1}Sb_2$) was

17   carried out by HRTEM (Modell: Technai G^2F^{30};STWIN) operating at 300 kV. The details of

18   TEM specimen preparation of Mg_3Sb_2 has been described elsewhere.[18, 20]

19

20   **2.3. Thermoelectric Properties**

21   The polished SPSed pellets of $Mg_{3-x}Zn_xSb_2$ ($0 \leq x \leq 0.1$) samples were used directly for thermal

22   diffusivity measurements parallel to the pressing direction by using a laser flash system

23   (Lineseis, LFA 1000) on disk-shaped thin specimens with approximate thickness of 1.5 mm and

24   12.7 mm diameter. The disc specimens used for thermal diffusivity were sprayed with a layer of

25   graphite in order to minimize errors due to emissivity. Specific heat was determined by a DSC

26   instrument (822^e Mettler Toledo). The thermal conductivity of all the samples was calculated

27   using the relation $\kappa = d \times C_p \times \rho$, where κ is the thermal conductivity, d the thermal

28   diffusivity, ρ the geometrical pellet density and C_p the specific heat capacity. The polished bars

29   of about $3 \times 2 \times 10$ mm were cut from the consolidated disks and are used to measure the

30   electrical conductivity and Seebeck coefficient in a direction perpendicular to the pressing

1 direction by employing commercial equipment (ULVAC, ZEM3) over the temperature range of

2 323 K to 773 K.

2.4. Hall measurement

4 Room temperature Hall Effect was carried out using the van der Pauw method. The Hall

5 coefficient was determined using an a.c. power supply of 29 Hz frequency and magnetic

6 induction of 0.9 T. The Hall carrier concentration (n_H) was calculated via $n_H = 1/eR_H$, where R_H

7 is the Hall coefficient and e is the electron charge. The Hall mobility (μ_H) was calculated by the

8 relation $\mu_H = \dfrac{\sigma}{n_H e}$.

2.5. Electronic Structure Calculations

10 In order to study the materials properties at an electronic level, First Principles calculations were

11 employed to study the electronic structure and transport properties of Mg_3Sb_2 using the full

12 potential linearized augmented plane wave (FP-LAPW) method as implemented in Wien2K suite

13 of programs.[30, 31] To model chemical disorder, we make use of a $2 \times 2 \times 2$ size supercell in which

14 one Mg atom is replaced by a Zn atom. Since there are two inequivalent Mg ions in Mg_3Sb_2,

15 calculations were carried out for both tetrahedral and octahedral site positions. To obtain the

16 equilibrium structure in terms of internal coordinates, the atomic positions were relaxed by using

17 a dampened Newton scheme, based on the minimization of Hellmann–Feynman forces to values

18 smaller than 5 meV Å^{-1}. Self-consistency was achieved when the variation in the total energies

19 between two consecutive iterations was smaller than 10^{-5} eV. The charge density was converged

20 to 10^{-2}e. The basis sets was constructed with $R_{MT}K_{max} = 7$, $G_{max} = 24$ and $l_{max} = 10$. The LAPW

21 sphere radii, (R_{MT}) for Mg and Sb were chosen to be $2.2a_o$, where a_o is the Bohr radius. The

22 Brillouin zone (BZ) integration was performed with 192 k-points distributed over the irreducible

23 wedge of the BZ. The magnitude of E_g is crucial and, hence we have used the modified Becke–

24 Johnson (mBJ) scheme to account for the exchange and correlation effects. It is observed that for

25 such system mBJ potential predict the band gaps with higher precision and is certainly better

26 than the conventional parameterization based on the local density approximation (LDA) and

27 generalized gradient approximation (GGA).[32-36] The transport properties were calculated within

28 the constant relaxation-time approximation of the Boltzmann transport equation, as implemented

29 in the BoltzTraP code.[37] Up to 4900 k-points in the BZ were used to perform the averaging.

3. Results:

3.1 Structure and Phase Analysis:

The phase purity of all the samples were verified before doing transport property measurements. Figure 2(a) presents the X-ray diffraction (XRD) patterns of sintered pellets of $Mg_{3-x}Zn_xSb_2$ ($0 \leq x \leq 0.1$). The XRD patterns show that all Zn substituted samples are single phase and can be indexed to $\beta-Mg_3Sb_2$ structure (JCPDS-00-003-0375) without any impurity or secondary phases. The cell constants were estimated by the POLSQ FOR-TRAN program.[38] The lattice parameters, a and c, for undoped Mg_3Sb_2 was determined as to be 4.563 and 7.229 Å, respectively. A nominal increase in the lattice parameters were observed with increasing Zn concentration. For x=0.1, a (c) was increased by 0.1% (0.06%). Such a trend is expected due the relatively larger ionic radii of Zn ($\cong 0.74$ Å) in comparison to Mg ($\cong 0.66$ Å). However, an opposite trend had been reported by Xin et al.[26] The linear increase in the lattice parameters are also in accordance with the Vegard's approximation. Note that in reference [Xin et al.][26] substantial amount of unreacted Sb was observed. Thus, clearly our adopted method of synthesis, involving high temperature SPS leaves no such trace of unreacted materials and thus certainly seems advantageous over the hot pressing method adopted by Xin et al.[26]
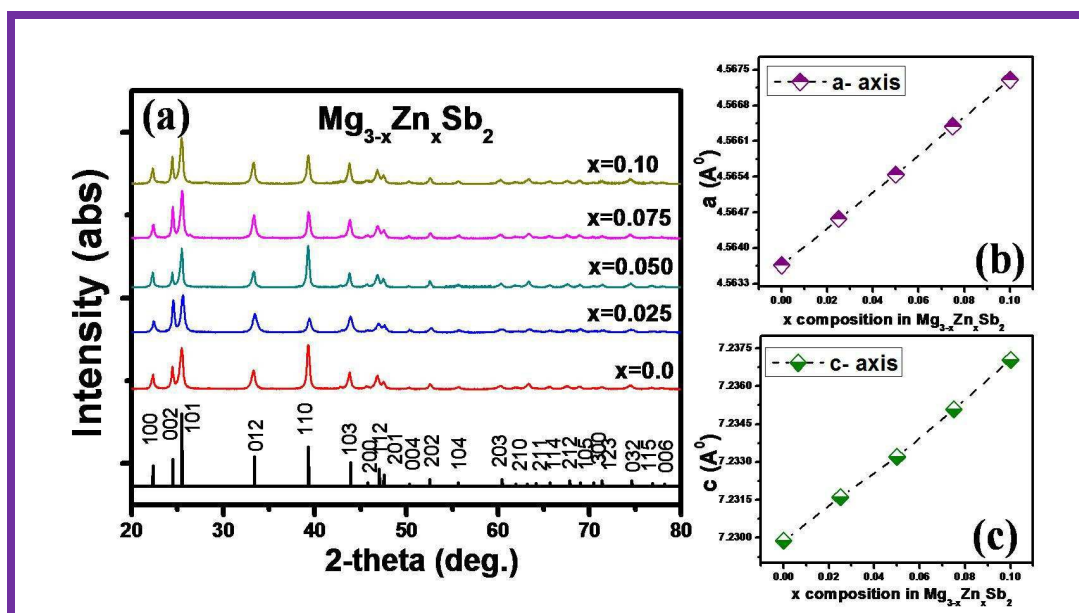
Figure 2: (a) XRD pattern of $Mg_{3-x}Zn_xSb_2$ ($0 \leq x \leq 0.1$) systems. The linear variation of the cell parameters a and c with increasing Zn concentration are shown in (b) & (c) respectively.

1

3.2. Transmission Electron Microscopy Investigation:

A detailed microstructure of the best performing $Mg_{2.9}Zn_{0.1}Sb_2$ sample has been carried out by HRTEM. The bright field electron micrographs obtained from the specimen of $Mg_{2.9}Zn_{0.1}Sb_2$ as shown in figure 3(a) infers to a polycrystalline structure throughout the volume of the material. The micrograph clearly reveals that the individual grains with sizes ranging from 7 to 70 nm are truly crystalline with stacking of different planes with random orientation. Corresponding selected area electron diffraction (SAED) pattern, as shown in the inset of figure 3 (a), further reveal a set of Debye rings with fine sharp spots overlapping on individual rings. The analysis of these rings reveals that the material exhibits a single phase of hexagonal structure with space group $P\bar{3}m1$ with a set of lattice planes h k l : $11\bar{2}0$, $20\bar{2}0$, $11\bar{2}4$, $21\bar{3}3$ having their respective inter planer spacing of 0.229, 0.198, 0.142, 0.127 nm. Several lattice scale images were recorded to understand the presence of different orientations of the crystallographic planes and their interface boundaries at an atomic level. Figure 3(b) presents one of the representative HRTEM image obtained from sample showing several grains orientated in direction of different planes of Mg_3Sb_2 and several joint interface boundaries. Interestingly, the lattices associated with grains of $Mg_{2.9}Zn_{0.1}Sb_2$ are little distorted together with some misfit type of dislocations at the interfaces as shown by arrows in figure 3 (b). These distortions at microscopic level are due to local strain induced by the Zn substitution at Mg site.

20
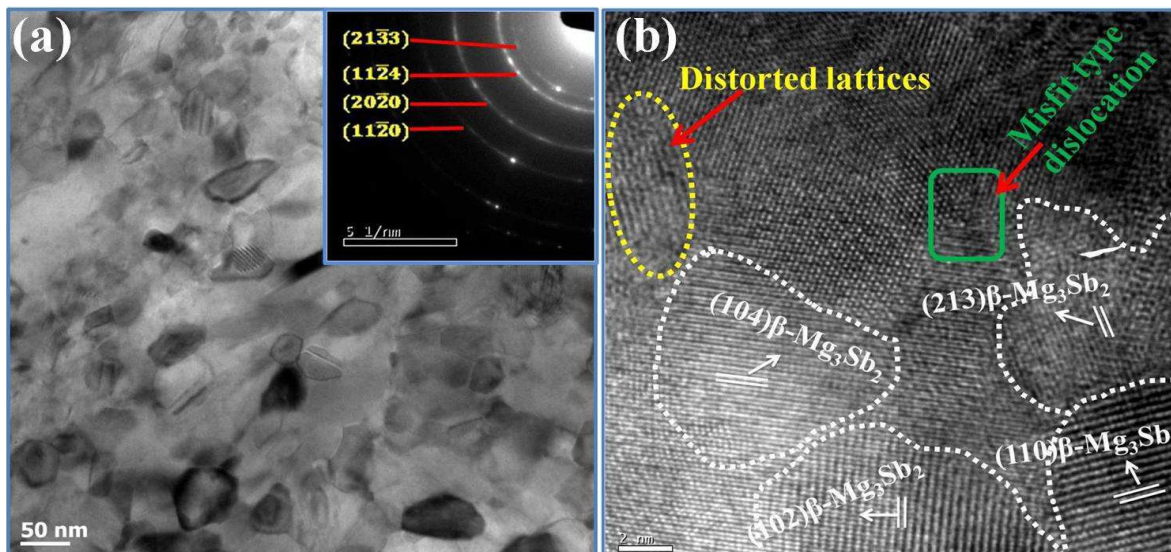
1 **Figure 3:** (a) TEM image of $Mg_{2.9}Zn_{0.1}Sb_2$ showing densely packed grains. The inset of figure

2 3(a) shows the SAED pattern of the sample, revealing the hexagonal symmetry, b) lattice scale

3 image of $Mg_{2.9}Zn_{0.1}Sb_2$ exhibiting the presence of different orientations of the crystallographic

4 planes and distorted lattices.

5 **3.3. Thermoelectric transport properties:**

6

7 3.3.1. Electrical conductivity (σ(T)) and carrier concentration (n)

8 Temperature dependent electronic transport properties of $Mg_{3-x}Zn_xSb_2$ ($0 \leq x \leq 0.1$) were

9 measured using the state-of-art techniques. In figure 4(a) we show the temperature dependence

10 of electrical conductivity σ (T) for all the sintered $Mg_{3-x}Zn_xSb_2$ ($0 \leq x \leq 0.1$) samples. All the

11 samples show semiconducting nature. Regardless of the temperature, the σ (T) of the Zn doped

12 samples is observed to be lower than that of the undoped Mg_3Sb_2. The decrease in σ (T) is

13 attributed to the decrease in n, apart from the disorder scattering of free charge carriers in the

14 system. The n deduced using the relation ($n_H = 1/R_H$ e) by the Hall effect measurements at room

15 temperature is shown in table 1. It is seen that n decrease with increasing Zn concentration. The

16 overall decrease in n for x=0.1 is $\cong$ 22 % in comparison to undoped Mg_3Sb_2. It is worth noting

17 that our room temperature σ (T) of Mg_3Sb_2 is 226.36 S m^{-1} which is nearly three orders of

18 magnitude higher than the value (~0.306 S m^{-1}) reported by Xin et al.[26] The relatively large σ (T)

19 is due to the highly densified and near stoichiometric samples obtained by spark plasma assisted

20 reaction sintering. It is generally understood that the uni-axial hot-pressing method, like those

21 adopted by Xin et al.[26] at very low pressure and low temperature, introduce large concentration

22 of defect centers leading to high carrier scattering and hence low σ (T).

23

$Mg_{3-x}Zn_xSb_2$	x=0	x=0.025	x=0.050	x=0.075	x=0.1
Carrier concentration (10^{19} cm^{-3})	2.40	2.29	2.10	2.01	1.96
Mobility ($cm^{-2}V^{-1}s^{-1}$)	5.54	5.31	5.44	5.42	5.22
m^*/m_o	0.7392	0.7695	0.7440	0.7432	0.7639

24

25 **Table 1:** The change in the carrier concentration with Zn concentration (x) in $Mg_{3-x}Zn_xSb_2$ ($0 \leq x$

1   ≤ 0.1) determined at room temperature using effect Hall measurements; $n_H = 1/R_H\,e$.

2   3.3.2. Seebeck coefficient, S(T)

3   In figure 4(b) we show the temperature dependence of S(T) for all sintered samples. The

4   positive values of S(T) over the measured temperature range indicate to p-type carriers which is

5   consistent with the sign of the charge carriers deduced from the Hall measurements. Common to

6   all samples, the absolute values of S(T) first increase and then decrease with increasing

7   temperature. The increase in S(T) is fundamentally attributed to the increasing number of

8   thermally excited carriers in the respective disordered systems, and the decrease in S, due to bi-

9   polar effects, where both electrons and holes participate in the transport properties. However,

10 two salient features are to be noted in S(T) (i) the increase in the peak maximum (S_{max}) with

11 increasing x in $Mg_{3-x}Zn_xSb_2$ and the shift in S_{max} towards low T. For example, while S_{max} for

12 x=0 is ~327 µV/K at T $\approx$ 673 K, for x = 0.1 S_{max} is ~415 µV/K at T $\approx$ 623 K. It is also found that

13 the shift in S_{max}(T) towards low T with increasing x is linear and is consistent with the variation

14 in $n(x)$. The increase in the magnitude of S_{max} with increasing x can be attributed to the

15 decreasing 'n' via Motts equation.[39] On the other hand, shift of S_{max} to lower T, suggests a

16 decrease in the materials band gap. Thus, isoelectronic doping of Zn at the Mg site appears to be

17 an effective way of optimizing the thermoelectric transport properties, in the mid temperature

18 range thermoelectric application.

19 We notice that the S(T) of parent Mg_3Sb_2 ($\approx$193.5 µVK^{-1} at room temperature) is much

20 smaller in comparison to those reported by Xin et al.[26] The opposite trend in σ(T) and S(T) is

21 consistent with the transport theory; and therefore unambiguously suggest that n plays an

22 important role in the materials transport properties.

23 The crucial electronic quantity that expresses the thermoelectric performance is the power

24 factor defined as $PF=\sigma S^2$. The temperature variation of PF is shown in figure 4c. The highest PF

25 is optimized for x=0.1 at 773 K which is 18 % larger than the undoped Mg_3Sb_2. Comparing room

26 temperature PF of Mg_3Sb_2 with earlier reports[16], it can be noted that the PF of Mg_3Sb_2 ($\sigma S^2 \approx$ 8.4

27 µWm^{-1}K^{-2}) in the present work is much higher than the value 0.13 µWm^{-1}K^{-2} reported by Xin et

28 al.[26]
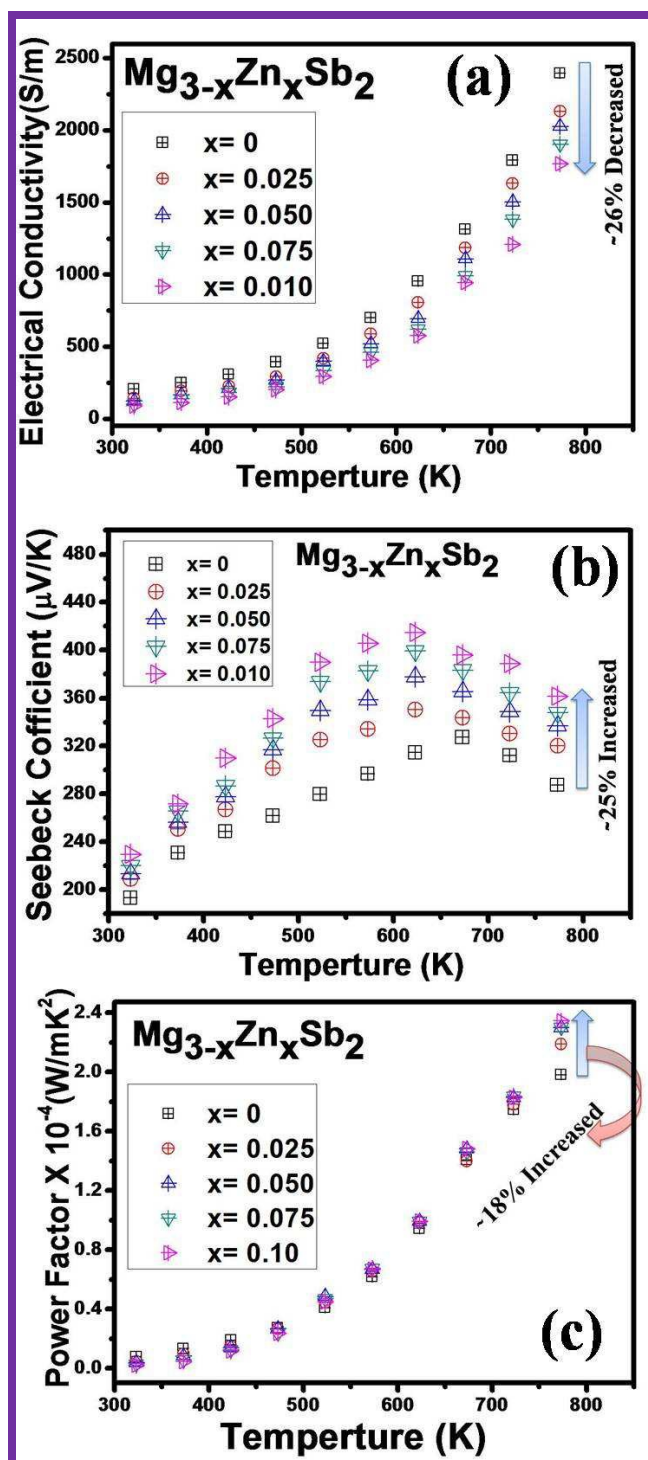
Figure 4: a) Temperature dependence of the electrical conductivity of $Mg_{3-x}Zn_x Sb_2$ ($0 \leq x \leq 0.1$) compounds. b) Temperature dependence of the Seebeck coefficient S(T) and c) Temperature dependent power factor for $Mg_{3-x}Zn_x Sb_2$ ($0 \leq x \leq 0.1$).

3.3.3. Thermal conductivity

1   The temperature dependence of thermal conductivity $\kappa(T)$ of $Mg_{3-x}Zn_xSb_2$ ($0 \leq x \leq 0.1$) are

2   presented in figure 5(a). We find that the $\kappa(T)$ decreases with increasing x in Mg_3Sb_2. Beyond,

3    $\kappa(T)$ decreases with increasing temperature for all x showing a T^{-1} type behavior. Since $\kappa(T)$ is

4   the sum of lattice thermal conductivity (κ_L) and electronic thermal conductivity κ_{el}, one may

5   expect κ_L to decrease with the increasing Zn concentration due to chemical disorder. The

6   relatively heavier Zn atoms introduce both mass fluctuation and strain field fluctuation scattering

7   for phonons due to the variation in both mass and size differences. Besides, κ_{el} would also be

8   expected to decrease due to decrease in $\sigma(T)$, following Wiedemann Franz Law. Comparing the

9   values of κ for both x=0 and x=1, we find an overall decrease by 18 % at 623 K. The systematic

10   variation in $\kappa(T)$ as a function of x in $Mg_{3-x}Zn_xSb_2$ ($0 \leq x \leq 0.1$) at 773 K is shown in figure 5

11   (b). It is worth mentioning that the relatively lower value of $\kappa(T)$ (~1.2 $Wm^{-1}K^{-1}$ at room

12   temperature) in Mg_3Sb_2 was reported by Xin et al.[26] which might be due to low density of the

13   sample obtained by conventional hot pressing.
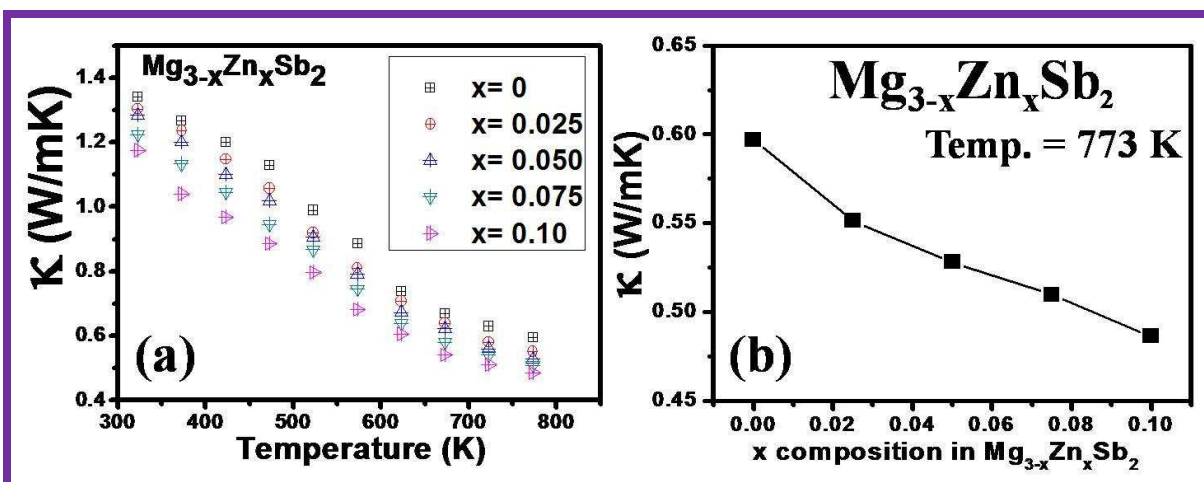
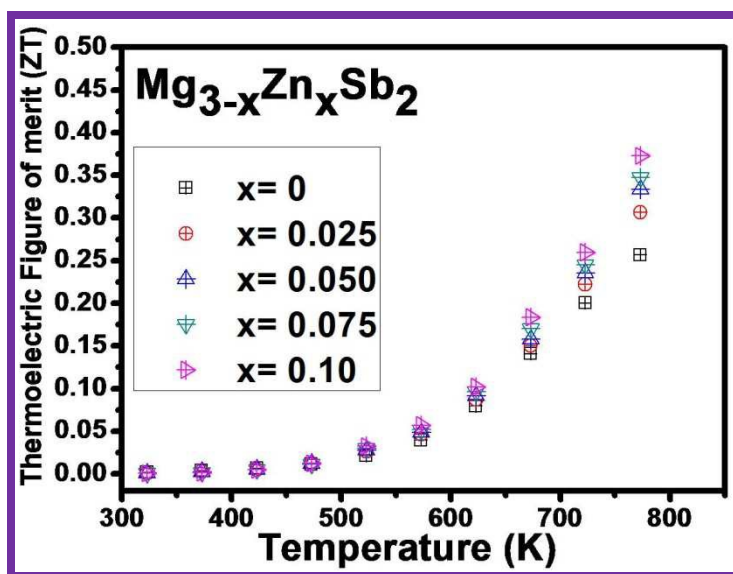15   **Figure 5:** a) Temperature dependence of the thermal conductivity κ (T) of $Mg_{3-x}Zn_x$ Sb_2 ($0 \leq x \leq$

16   0.1) compounds, b) variation in the thermal conductivity κ (T) of all the $Mg_{3-x}Zn_xSb_2$ ($0 \leq x \leq$

17   0.1) samples at 773 K with increasing x.

18   3.3.5. Thermoelectric figure-of-merit (ZT)

19   Using S(T), $\sigma(T)$ and $\kappa(T)$, we compute the materials ZT according to reference 1. The variation

20   of ZT for various x with temperature is shown in figure 6. The maximum ZT $\simeq$ 0.37 at 773 K

21   was optimized for x=0.1 which is $\simeq$ 42% larger than that for the undoped Mg_3Sb_2 (ZT $\simeq$ 0.26 at

1   773 K). The enhanced ZT is attributed both to the simultaneous increase in the materials PF and

2   the decrease in $\kappa(T)$. The increase in the PF and reduced $\kappa(T)$ can be fundamentally assigned to

3   the optimal tuning of n in Zn doped systems. Interestingly, the room temperature ZT of Mg_3Sb_2

4   is determined as ≈ 0.0018 which is nearly 20 times higher than the value (ZT~0.000875 at room

5   temperature) reported earlier.[26]

6


7

8   **Figure 6:** Temperature dependence of thermoelectric figure of merit of $Mg_{3-x}Zn_xSb_2$ ($0 \leq x \leq$

9   0.1) samples.

10   ## 4. First-Principles Calculations

11   **A. Energetics**

12   Having two inequivalent Mg ions, namely those at the octahedral and tetrahedral sites of the

13   hexagonal cell, it becomes rudimentary to check the energetically preferable site for Zn

14   substitutions in Mg_3Sb_2. Thus, in a supercell of $2 \times 2 \times 2$ dimensions we substitute a Mg(I) ion

15   by Zn and compare its fully relaxed total energy with that of a Mg(II) ion substituted with Zn.

16   Comparison of total energies show that Zn prefers the tetrahedral site substitution i.e., into the

17   $(Mg_2Sb_2)^{2-}$ covalently bonded motif. The tetrahedral substitution is lower in energy by $\simeq 90$

18   meV/f.u in comparison to the octahedral site substitution. Thus, we find that the first-principles

19   deduced structural stability of Zn substitutions of Mg(II) ions at the tetrahedral site is consistent

20   with the earlier experimental reports.[18]
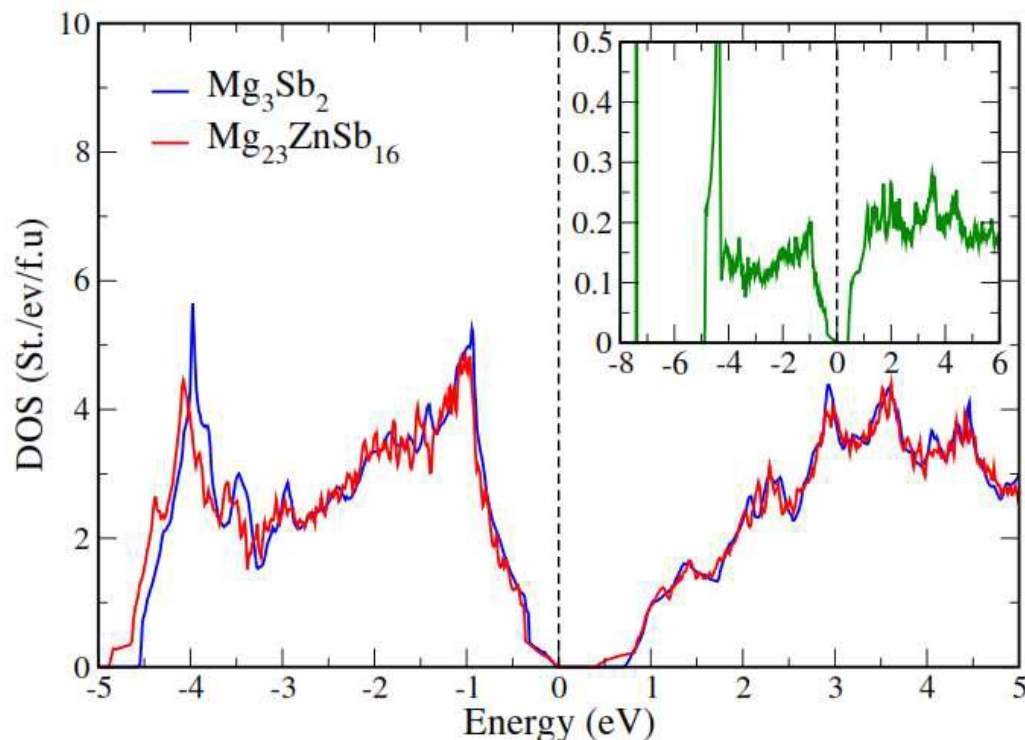
1

2   **Figure 7:** The mBJ-GGA generated total density of states of $Mg_{23}ZnSb_{16}$ shown in comparison

3   with the undoped Mg_3Sb_2. In the inset shown is the Zn density of states expressed in units of

4   St./ev/atom. The vertical line through zero energy represents the reference Fermi energy.

5   Theoretical calculations also have shown that the nature of bonding associated with Mg(I) and

6   Mg(II) in Mg_3Sb_2 are very different.[18] Based on bonding analysis and band structure, it was

7   shown that Mg at the octahedral sites is purely ionic while those at tetrahedral sites display

8   covalent characteristics. Thus, the site preference of Zn ions in the covalent substructure, could

9   be attributed to stronger hybridization due to its much larger spatial extend of the valence 4s

10   orbitals in comparison to the Mg 3s orbitals. This also partly explains the reduction in $\sigma(T)$ in

11   $Mg_{3-x}Zn_xSb_2$, as increased orbital overlap would spatial confine electrons thereby reducing the

12   density of free charge carriers in the system. Furthermore, the reduction in $\sigma(T)$ could also be

13   well associated with chemical disorder which introduce carrier scattering in the $(Mg_{2-x}Zn_xSb_2)^{2-}$

14   motifs.

15

16   **B. Electronic structure**

17   Figure 7 shows the density of states of $Mg_{23}ZnSb_{16}$ compared with that of the undoped

1   Mg_3Sb_2. The overall features of the valence band spectral features appear similar in both

2   systems. In the energy window ranging from −5 eV to E_F (E=0 eV), the spectra is dominated by

3   the Sb 5p with little admixture of the cation (Mg/Zn) s states. On the other hand, the lower

4   conduction band is dominated by Mg (Zn) 3s (4s) states of the tetrahedral site in the respective

5   systems. However, with Zn substitutions, the magnitude of the energy band gap, decreases.

6   While for Mg_3Sb_2, the E_G is estimated to be 0.7 eV, with Zn substitutions the band gap reduces

7   to 0.4 eV.
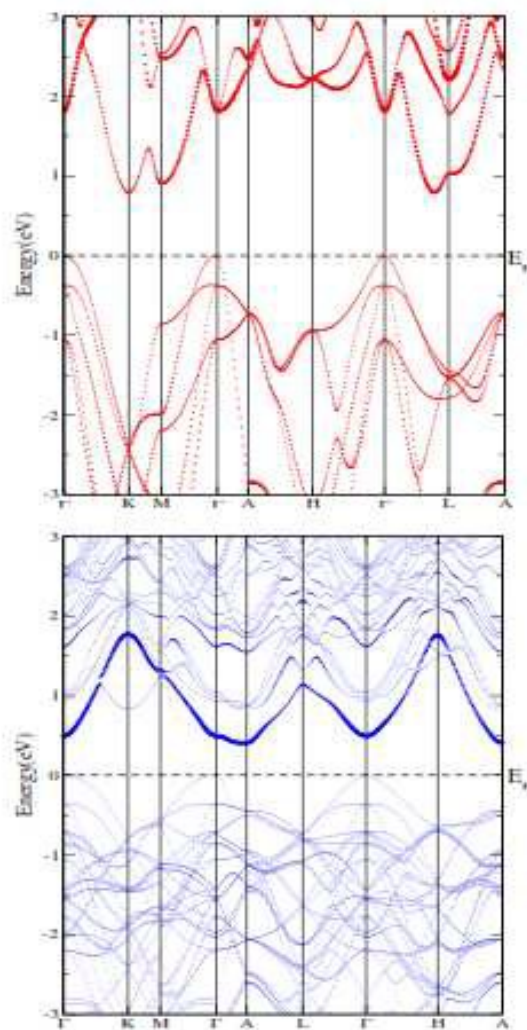
8

9   **Figure 8:** The mBJ-GGA generated band structure of Mg_3Sb_2 (blue curve) and $Mg_{23}ZnSb_{16}$ (red

10   curve) as obtained from the FP-LAPW method of calculations. In the inset shown is the atom

11   resolved Zn partial density of states, in units of St./eV/atom. The broken line through zero energy

12   represents the Fermi energy.

13

1   The decrease in the band gap can be associated to the lower energy of the Zn 4s orbitals as

2   compared to the Mg 3s orbital which is a common mechanism to the difference in the band gap

3   between the semiconductors based on Mg and Zn. For example, while the MgS, MgSe and MgTe

4   systems display a band gap of 4.45, 3.59 and 3.49 eV, respectively,[40,41] the band gap associated

5   with ZnS, ZnSe and ZnTe are 3.8, 2.82 and 2.39 eV, respectively.[42-45]

6   To study the nature of band dispersion, we shown in figure 8 the band structure of Mg_3Sb_2 and

7    $Mg_{23}ZnSb_{16}$. For the detailed description of the band structure of un-doped Mg_3Sb_2 we refer to

8   our previous work.[18] However, to illustrate the changes brought out by Zn substitutions in

9   Mg_3Sb_2, we show the band structure of the undoped Mg_3Sb_2, as well. Note that the increased

10   number of bands reflects to the size of the supercell used for the disorder modeling. Although

11   being isoelectronic and isostructural, one observes significant changes in the band structure of

12   the two systems. Apart from the decrease in the band gap, one observes that the Zn 4s bands,

13   highlighted in the fat band representation in figure 8, occupy the lowest of the conduction band

14   region.

15   In order to study the change in the dispersion of bands with Zn substitutions, we compare the

16   Γ-A and Γ-M segments of the hexagonal BZ. These BZ directions, when mapped in real space

17   correspond to the vectors in the a-b (in-plane) and along the hexagonal c direction. In Mg_3Sb_2,

18   the top of the valence band is composed of heavy bands (along Γ–M) and light bands (Γ–A and

19   H–L directions). One also find similar characteristics of band dispersion at $\simeq$ 0.4 below E_F

20   where non-parabolic dispersion of bands could be seen along various other BZ segments.

21   One observes that the dispersion of the Sb 5p bands along Γ-A in Mg_3Sb_2 (E = E_F to E $\simeq$ 3 eV)

22   is significantly reduced in $Mg_{23}ZnSb_{16}$ (E = E_F to E $\simeq$ 1.2 eV). Similar changes are also

23   observed along the Γ-M direction, where the Sb 5p bands which extend from E_F to E $\simeq$ 2 eV is

24   relatively confined in $Mg_{23}ZnSb_{16}$ from E_F to E $\simeq$ 0.6 eV. The dramatic reduction in the E(k)

25   dispersion infers to an increase in the effective mass of the system. In the regime of acoustic

26   phonon scattering of charge carriers, the mobility and the effective mass are related by $\mu \propto$

27    $(m^*_e)^{-5/2}$. Thus, it is evident from the materials band structure that the mobility of the charge

28   carriers is considerably decreased with Zn substitutions. Together with reduction in the carrier

29   concentration as inferred from our experiments, these electronic structure effects explain the

30   reduction in σ and enhancement of S in Zn substituted Mg_3Sb_2 systems.

31

1   **C. Theoretical Calculation of S (n,T)**

2   In figure 9, we show the temperature dependent variation of S(T) for the in-plane and c-

3   axis directions. The hexagonal symmetry of the system implies that the Seebeck tensor elements

4   will be diagonal and that the S_{ii}; i = x (y) and i = z would be different. The temperature

5   dependence of both in-plane S_{xx} (S_{yy}) and that along the c-axis, S_{zz} contribution to the S(T) are

6   shown in figure 9. The overall trend as calculated from the Boltzmann's equations are consistent

7   with the experiments, i.e., S(T) initially increases with increasing temperature and falls beyond

8   certain optimum temperature.
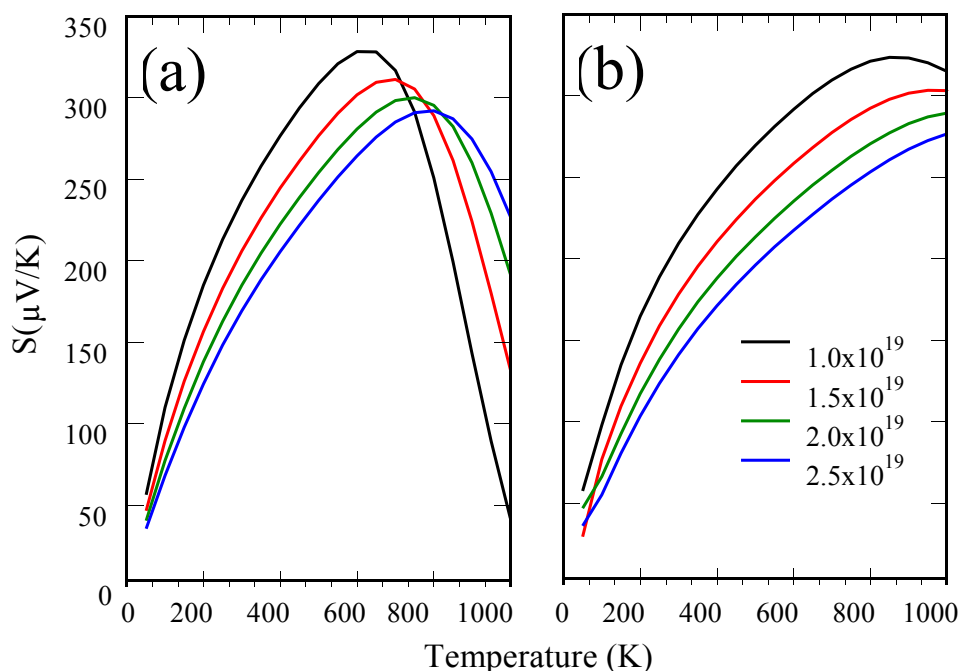
33   **Figure 9:** (color online) The calculated variation of Seebeck coefficient as a function of

34   temperature as indicated. (a) in-plane (b) out of plane respectively, for various electron charge

35   concentration. Here, S is expressed in units of μV/K.

38   The decrease in the S(T) at high temperatures are attributed to bipolar effects. However,

39   the salient features in the variation of S(n, T), which are also observed in the experiments, are

40   reproduced in the theoretical calculation, as well, i.e., (i) the magnitude of the peak maximum in

41   S(T) increases with decreasing n and (ii) that the peak maximum in S(T) shifts towards lower

1 temperatures with decreasing n. The increasing peak maximum of S(T) basically indicates to

2 high effective mass (m_e*) of the system and is consistent with the Mott relation S$\propto m_e$*. That,

3 m_e* increases with Zn substitutions are also evident from the band structure. For example, the

4 band along the Γ- M direction in undoped Mg_3Sb_2 is more dispersed in comparison to the Zn

5 substituted Mg_3Sb_2; indicating to higher m_e*.

6

7 5. Discussion

8 Following the band structure, for p-type doping, the dependence of S(T) with n can be described

9 in a single band model for a heavily doped semiconductor. Considering the acoustic phonon

10 scattering λ =0, S (n,T) can be written as[46]

11 $$S(n,T) = \frac{8\pi^2 K_B^2}{3eh^2} m_e^* T \left(\frac{\pi}{3n}\right)^{\frac{2}{3}} \dots\dots\dots\dots\dots\dots\dots\dots\dots\dots\dots\dots\dots\dots\dots\dots\dots\dots\dots\dots\dots\dots\dots\dots 1)$$

12 Infact, the linear dependence of S (T) with temperature for single carrier conduction is found

13 below T < 600 K. In this temperature range, we estimate the m_e* the values of which are shown

14 in table 1. A more detailed description of this model can be found in other reports.[47, 48] An

15 effective mass corresponding to 0.7639 m_e was used to calculate the Pisarenko relation at room

16 temperature (figure 10(a)). Evidently, the good fit of S (T = 323 K) with n suggest the validity of

17 a single parabolic band model to describe the electronic transport of $Mg_{3-x}Zn_xSb_2$ ($0 \leq x \leq 0.1$) at

18 temperatures below 600 K. Based on the above analysis we find that transport properties of Zn

19 substitution in Mg_3Sb_2 is mainly monitored by the n.

20 Considering the carrier concentration dominated transport in Zn substituted Mg_3Sb_2, we

21 assume the effective mass to be constant with the temperature, with n computed using equation

22 1, we plot the variation of S (T) for various temperature. Unlikely to the Pisarenko plot at room

23 temperature where all the points were lying on the line, we noticed a large deviation in the trend

24 of Pisarenko plot, inferring that the effective mass (m_e*) at higher temperature cannot be similar

25 to that at room temperature.

26
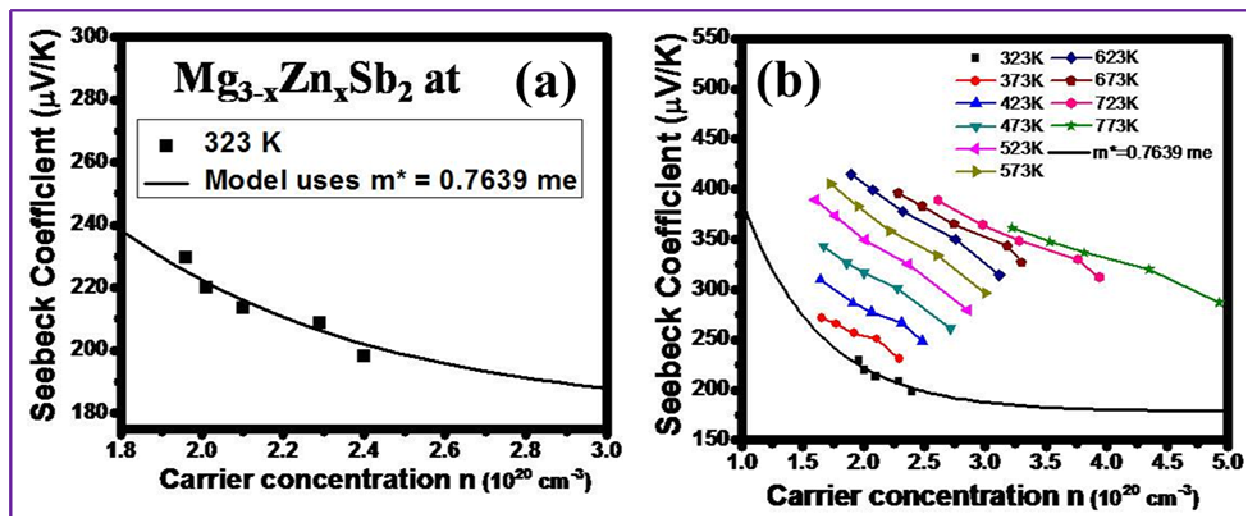
Figure 10: a) Pisarenko plot at 323 K showing the dependence of Seebeck coefficient on the carrier concentration (solid line). The experimental data lie on or near the curve (single parabolic band model) generated for $m_e^*=0.7639\ m_e$ for x=0.1, suggesting all the samples have almost equal effective masses at room temperature; b) Pisarenko plot for room temperature to 773 K with fix $m^*=0.7639\ m_e$ showing the deviation from the single parabolic band model.

Our experiments with the doped Mg_3Sb_2 materials reveals that these are potentially those Zintl compounds which are prototype to achieve the "phonon-glass electron-crystal" characteristics, required for the optimization of thermoelectric performance. The structure of Zintl Mg_3Sb_2 is manifested in the form of two substructures, namely the cation layer composed of Mg (I) ions which are ionic, and the covalent bound $(Mg_2Sb_2)^{2-}$ anion network. Substitutions in the Mg (I) layer could lead to long periodic structure, as like $MnSi_{1.75}$,[49, 50] with large number of atoms in the unit-cell. If substitutions are accomplished at this octahedral site with heavy mass elements one could well expect a decrease in the materials thermal conductivity due to mass fluctuation induced phonon scattering. On the other hand, the anionic substructure largely dictates the electrical transport properties of the material. It appears that due to the strong covalent bonding, isoelectronic substitutions are energetically favorable in the anion substructure. It is also interesting to note that with increasing substituent concentration, say Sm substitutions,[51] super-structures form, which due to their increased volume and number of atoms in the unit-cell would also be effective in reducing the materials thermal conductivity.

A combination of both heavy and light bands would be crucial to optimize the electronic

1   performance of a thermoelectric system. Band structure of Mg_3Sb_2 clearly reveals both such

2   band types in the near vicinity of its Fermi energy. Interestingly, we find that an appropriate

3   substituent could be introduced in the anionic substructures which have separate effects on these

4   bands. While Bi ions, which are isoelectronic to Sb ions, when introduced in small

5   concentrations in Mg_3Sb_2 as in our previous report[8], σ remained more or less unchanged,

6   however, with an enhancement in S (T). On the other band, isoelectronic Zn doping at the Mg

7   site of the $(Mg_2Sb_2)^{2-}$ anion substructure resulted in a decrease in σ, however with an increase in

8   S. We note that Mg_3Bi_2 which is isostructural with Mg_3Sb_2 is semi-metallic. Thus, it may be

9   expected that multi-site doping in the $(Mg_2Sb_2)^{2-}$ anion substructure of these Zintl based

10   materials would be an effective way to optimize the thermoelectric performance. Our

11   experiments show that the phonon-glass electron-crystal aspect, could be accomplished via

12   controlling the n by appropriate dopants to enhance the PF, and heavy ion substitution such as

13   rare-earths at Mg site could decrease κ (T) via mass fluctuation scattering.

14

6. Conclusions:

16   Single phase $Mg_{3-x}Zn_xSb_2$ ($0 \leq x \leq 0.1$) compounds were successfully synthesized by employing

17   the spark plasma assisted sintering reaction. The Zn^{2+} substitution on Mg^{2+} site in the anionic

18   framework $(Mg_2Sb_2)^{2-}$ results in an optimal control over the carrier concentration. Such

19   tunability of n drives the system to achieve a ZT of 0.37 at 773 K in $Mg_{2.9}Zn_{0.1}Sb_2$, which is

20   ≃ 42 % higher in comparison with the undoped Mg_3Sb_2. This enhancement in ZT is not only due

21   to the optimization of n but also due to the reduction in thermal conductivity via mass fluctuation

22   scattering. We understand that multi-site doping in the anionic framework of this Zintl phase

23   compounds would be an effective strategy to optimize high ZT via electronic structure

24   modification and mass fluctuation scattering. Future Avenue of the research along these

25   perspective are currently under consideration.

Acknowledgement

4. **Reference:**

5. 1. The thermoelectric performance of a solid state material on the temperature (T) scale is

6. gauged in terms of its figure of merit, $ZT = \frac{S^2 \sigma}{\kappa} T$, where S is the Seebeck coefficient, σ

7. the electrical conductivity and κ (= κ_L+LσT) the total thermal conductivity, which has

8. contributions from both electronic (κ_{el} =LσT ; L being the Lorenz number) and lattice

9. (κ_L).

10. 2. S. Perumal, S. Roychowdhury, D. S. Negi, R. Datta, K. Biswas, *Chemistry of Materials*,

11. 2015, **27**, 7171-7178.

12. 3. S. N. Guin, J. Pan, A. Bhowmik, D. Sanyal, U. V. Waghmare, K. Biswas, *Journal of the*

13. *American Chemical Society,* 2014, **136**, 12712-12720.

14. 4. S. Roychowdhury, U. S. Shenoy, U. V. Waghmare, K. Biswas, *Angewandte Chemie,*

15. 2015,***127***, 15456-15460.

16. 5. A. Banik, K. Biswas, *Journal of Materials Chemistry A,* 2014, **2**, 9620-9625.

17. 6. D. K. Misra, A. Rajput, A. Bhardwaj, N. S. Chauhan, S. Singh, *Applied Physics Letters,*

18. 2015, ***106***, 103901.

19. 7. D. K. Misra, A. Bhardwaj, and S. Singh. *Journal of Materials Chemistry A,* 2014,

20. **30**,11913-11921.

21. 8. A. Bhardwaj, and D. K. Misra, *Journal of Materials Chemistry A,* 2014, **48**, 20980-

22. 20989.

23. 9. A. Bhardwaj, N. S. Chauhan, B. Sancheti, G. N. Pandey, T. D. Senguttuvan, D. K.

24. Misra, *Physical Chemistry Chemical Physics,* 2015, ***17***, 30090-30101.

25. 10. A. Bhardwaj, D. K. Misra, J. J. Pulikkotil, S. Auluck, A. Dhar, and R. C. Budhani.

26. *Applied Physics Letters,* 2012,***101***,133103.

27. 11. D. K. Misra, S. Sumithra, N. S. Chauhan, W. M. Notling, P. F. P. Poudeu, and Kevin L.

28. Stokes, *Materials Science in Semiconductor Processing,* 2015, **40**, 453-462.

29. 12. S. R. Brown, S. M. Kauzlarich, F. Gascoin, G. J. Snyder, *Chem. Mater.*, 2006, **18**, 1873.

13. G. J. Snyder, M. Christensen, E. Nishibori, T. Caillat, B. B. Iversen, *Nature Mater.*, 2004, **3**, 458.

14. A. Bhardwaj, A. K. Shukla, S. R. Dhakate, D. K. Misra, *RSC Adv.* 2015, **5**,11058.

15. A. Bhardwaj, N. S. Chauhan, D. K.Misra, *Journal of Mater. Chem. A.,* 2015, **3**,10777.

16. S. M. Kauzlarich, S. R. Brown, G. J. Snyder, *Dalton Trans.*, 2007, **41**, 2099.

17. S. M. Kauzlarich, *Chemistry, Structure, and Bonding of Zintl Phases and Ions*, VCH Publishers, New York, 1996.

18. A. Bhardwaj, D. K. Misra, J. J. Pulikkotil, A. K. Shukla, A. Rajput, A. K. Srivastava, Govind, S. Auluck, A. Dhar, R. C. Budhani, *RSC Adv.,* 2013, **3**, 8504.

19. S. K. Bux, A. Zevalkink, O. Janka, D. Uhl, S. Kauzlarich, G. J. Synder, J. P. Fleurial, *J. Mater. Chem. A*, 2014, **2**, 215.

20. A. Bhardwaj, D. K. Misra, *RSC Adv.*, 2014, **4**, 34552.

21. A cubic bixbyite structure, referred as α phase, proto-typical of Mn_2O_3 is the high temperature phase and be-low $\simeq$1200 K, a structural phase transition to hexagonal phase (the β phase).

22. C. Zheng, R. Hoffmann, R. Nesper, and H. G. Schnering, *J. Am. Chem. Soc.*, 1986, **108**, 1876.

23. G. Busch, F. Hulliger, V. Winkler, *Helc. Phys. Acta,* 1954, **27**, 249.

24. J. H. Bredt, L. F. Kendall, Proceedings—IEEE/AIAA 1966.

25. C. L. Condron, S. M. Kauzlarich, F. Gascoin, G. J. Snyder, *J. of Sol. Stat. Chem.* 2006, **179**, 2252.

26. H. X. Xin, X. Y. Qin, J. H. Jia, C. J. Song, K. X. Zhang, J. Zhang, *J. Phys. D: Appl. Phys.* 2009, **42**,165403.

27. T. Kajikawa, N. Kimura, T. Yokoyama, *Proceedings of the 22nd International Conference on Thermoelectrics* 2003, **305**.

28. D. M. Verbrugge, J. B. Van Zytveld, *J. Non-Cryst. Solids,* 1993, **736**, 156.

29. D. J. Singh, D. Parker, *J. of Appl. Phys.,* 2013, **114**, 143703.

30. P. Blaha, K. Schwarz, G. K. H. Madsen, D. Kvasnicka, J. Luitz, *WIEN2k- An Augmented Plane Wave + Local Orbitals Program for Calculating Crystal Properties, TU Wien, Vienna, Austria,* **2001**.

31. K. Schwarz, P. Blaha, *Comput. Mater. Sci.,* 2003, **28**, 259.

32. Y. Imai, A. Watanabe, *J Mater Sci.,* 2006, **41**, 2435–2441.

33. F. Ahmadpour, T. Kolodiazhnyi, Y. Mozharivskyj, *J. of Sol. Stat. Chem.*, 2007, **180**, 2420–2428.

34. J. J. Pulikkotil, S. Auluck, *J. of alloys and compounds*, 2015, **626**, 208.

35. J. J. Pulikkotil, D. J. Singh, S. Auluck, M. Saravanan, D. K. Misra, A. Dhar, R. C. Budhani*, Phys. Rev. B.,* 2012, **86**, 155204.

36. J. J. Pulikkotil, S. Auluck, *AIP advances*, 2015, **5**, 037145.

37. G. K. H. Madsen, D. J. Singh, *Comput. Phys. Commun.,* 2006, **175**, 67.

38. D. Keazler, D. Cahen, J. Lbers, *POLSQ FORTRAN program*, IL: Northwestern University Evanston, **1984**.

39. N. F. Mott, H. Jones, The Theory of the Properties of Metals and Alloys (Dover, New York) **1958**.

40. H. Okuyama, Y. Kishita, A. Ishibashi, *Phys. Rev. B,* 1998, **57**, 2257.

41. M. T. Litz, K. Watanabe, M. Korn, H. Ress, U. Lunz, W. Ossau, A. Waag, G. Landwehr, T. Walter, B. Neubauer, D. Gerthsen, U. Schssler, *J. Cryst. Growth*, 1996, **159**, 54.

42. R. A. Pollak, L. Ley, S. P. Kowalczyk, D. A. Shirley, J. Joannopoulos, D. J. Chadi, M. L. Cohen, *Phys. Rev. Lett.* 1973, **29**, 1103.

43. W. D. Grobman, D. E. Eastman, *Phys. Rev. Lett.* 1972, **29**, 1508.

44. H. Venghaus, *Phys. Rev. B* 1979, **19**, 3071.

45. R. G. Lempert, K. C. Hass, H. Ehrenreich, *Phys. Rev. B* 1987, **36**, 1111.

46. M. Cutler, J. F. Leavy, R. L. Fitznatrick, *Phys. Rev. A* 1964, **133**, 1143.

47. A. F. May, E. S. Toberer, A. Saramat, G. J. Snyder, *Phys. Rev. B* 2009, **80**, 125205.

48. E. S. Toberer, A. Zevalkink, N. Crisosto, G. J. Snyder, *Adv. Funct. Mater.* 2010, **20**, 4375.

49. J. M. Higgins, A. L. Schmitt, I. A. Guzei, S. Jin , *J. Am. Chem. Soc.*, 2008, ***130*** (47), 16086−16094.

50. Z. Zamanipoura, X. Shia, M. Mozafarib, J. S. Krasinskia, L. Tayebib, D. Vashaeea *Ceramics International*, 2013, **39**, 3.

51. S. Gupta , A. K. Ganguli, J. D. Corbett, Inorg. Chem., 2006, **45**, 8175−8178.